

1 Long-duration gamma-ray emissions from 2007 and
2 2008 winter thunderstorms

H. Tsuchiya,¹ T. Enoto,² S. Yamada,³ T. Yuasa,³ K. Nakazawa,³ T.

Kitaguchi,⁴ M. Kawaharada,⁵ M. Kokubun,⁵ H. Kato,¹ M. Okano,¹ and K.

Makishima³

arXiv:1102.4024v1 [physics.ao-ph] 19 Feb 2011

3 **Abstract.** The Gamma-Ray Observation of Winter THunderclouds (GROWTH)
4 experiment, consisting of two radiation-detection subsystems, has been op-

H. Tsuchiya, High-energy Astrophysics Laboratory, Riken, 2-1, Hirosawa, Wako, Saitama 351-0198, Japan. (htsuchiya@riken.jp)

T. Enoto, Kavli Institute for Particle Astrophysics and Cosmology, Department of Physics and SLAC National Accelerator Laboratory, Stanford University, Stanford, CA 94305, USA (enoto@stanford.edu)

S. Yamada, Department of Physics, University of Tokyo, 7-3-1, Hongo, Bunkyo-ku, Tokyo 113-0033, Japan. (yamada@juno.phys.s.u-tokyo.ac.jp)

T. Yuasa, Department of Physics, University of Tokyo, 7-3-1, Hongo, Bunkyo-ku, Tokyo 113-0033, Japan. (yuasa@juno.phys.s.u-tokyo.ac.jp)

K. Nakazawa, Department of Physics, University of Tokyo, 7-3-1, Hongo, Bunkyo-ku, Tokyo 113-0033, Japan. (nakazawa@phys.s.u-tokyo.ac.jp)

T. Kitaguchi, Division of Physics, Mathematics, and Astronomy, California Institute of Technology, 1200 East California Boulevard, Pasadena, CA 91125, USA (kitaguti@caltech.edu)

M. Kawaharada, Department of High Energy Astrophysics, Institute of Space and Astronautical Science, JAXA, 3-1-1, Chuo-ku, Sagamihara, Kanagawa 252-5210, Japan. (kawaharada@astro.isas.jaxa.jp)

M. Kokubun, Department of High Energy Astrophysics, Institute of Space and Astronautical Science, JAXA, 3-1-1, Chuo-ku, Sagamihara, Kanagawa 252-5210, Japan. (kokubun@astro.isas.jaxa.jp)

H. Kato, High-energy Astrophysics Laboratory, Riken, 2-1, Hirosawa, Wako, Saitama 351-0198,

erating since 2006 on the premises of Kashiwazaki-Kariwa nuclear power plant
located at the coastal area of Japan Sea. By 2010 February, GROWTH de-
tected 7 long-duration γ -rays emissions associated with winter thunderstorms.
Of them, two events, obtained on 2007 December 13 and 2008 December 25,
are reported. On both occasions, all inorganic scintillators (NaI, CsI, and BGO)
of the two subsystems detected significant γ -ray signals lasting for >1 minute.
Neither of these two events were associated with any lightning. In both cases,
the γ -ray energy spectra extend to 10 MeV, suggesting that the detected γ -
rays are produced by relativistic electrons via bremsstrahlung. Assuming that
the initial photon spectrum at the source is expressed by a power-law func-
tion, the observed photons can be interpreted as being radiated from a source
located at a distance of 290 – 560 m for the 2007 event and 110 – 690 m
for the 2008 one, both at 90% confidence level. Employing these photon spec-
tra, the number of relativistic electrons is estimated as $10^9 - 10^{11}$. The es-
timation generally agrees with those calculated based on the relativistic run-
away electron avalanche model. A GROWTH photon spectrum, summed over
3 individual events including the present two events and another reported

Japan. (hkato@riken.jp)

M. Okano, High-energy Astrophysics Laboratory, Riken, 2-1, Hirosawa, Wako, Saitama 351-
0198, Japan. (mokano@crab.riken.jp)

K. Makishima, Department of Physics, University of Tokyo, 7-3-1, Hongo, Bunkyo-ku, Tokyo
113-0033, Japan. (maxima@phys.s.u-tokyo.ac.jp)

22 previously, has similar features including a cut-off energy, to an averaged spec-
23 trum of terrestrial gamma-ray flashes.

1. Introduction

24 Nonthermal X-ray and γ ray emission, typically lasting for a few seconds to ~ 10
25 minutes, has been observed from thunderstorm activity, with detectors on board an air-
26 plane [McCarthy and Parks, 1985] and a balloon [Eack et al., 1996, 2000], high-mountain
27 detectors [Suszcynsky et al., 1996; Brunetti et al., 2000; Chubenko et al., 2000; Alexeenko
28 et al., 2002; Muraki et al., 2004; Torii et al., 2009; Tsuchiya et al., 2009; Chilingarian et al.,
29 2010], and ground-based ones [Torii et al., 2002; Tsuchiya et al., 2007]. Interestingly, they
30 do not appear to clearly coincide with lightning processes such as stepped leaders or re-
31 turn strokes. In contrast, much shorter energetic radiation bursts, lasting only for tens
32 of milliseconds or less, are often associated with lightning discharges. Though not neces-
33 sarily homogeneous, they include terrestrial gamma-ray flashes (TGFs) [Fishman et al.,
34 1994; Smith et al., 2005; Grefenstette et al., 2009; Briggs et al., 2010; Connaughton et al.,
35 2010; Marisaldi et al., 2010a, b], natural lightning [Moore et al., 2001; Dwyer et al., 2005;
36 Howard et al., 2008; Yoshida et al., 2008; Chubenko et al., 2009], and rocket-triggered
37 ones [Dwyer et al., 2003, 2004a, b].

38 In this way, it has recently become clear that apparently two types of radiation bursts
39 with distinct duration are associated with thunderstorm activity. Although it is uncertain
40 whether or not these two types have a common source mechanism, recent observations
41 as well as theoretical works generally suggest that these bursts, especially short-duration
42 ones, are produced by processes involving acceleration and multiplication of a background
43 population of electrons.

44 Various numerical kinetic calculations [*Gurevich et al.*, 1992; *Roussel-Dupré et al.*, 1994;
45 *Bell et al.*, 1995; *Lehtinen et al.*, 1996; *Gurevich et al.*, 1997; *Milikh and Valdia*, 1999; *Gure-*
46 *vich et al.*, 2007; *Roussel-Dupré et al.*, 2008] and Monte Carlo simulations [*Lehtinen et al.*,
47 1999; *Dwyer*, 2003; *Babich et al.*, 2005, 2007] commonly indicate that most of prompt non-
48 thermal photons from lightning discharges are radiated, via bremsstrahlung, by relativistic
49 electrons, which in turn are produced through mechanism involving relativistic runaway
50 electron avalanche (RREA): some seed electrons, produced by e.g. cosmic rays, can be
51 accelerated into relativistic regime if they can gain energies from the high electric fields in
52 thunderclouds fast enough to overcome their total energy losses, due mainly to ionization.
53 Then, they collide with air molecules and ionize them. Some of the faster newborn sec-
54 ondary electrons are also accelerated to higher energies, hence increasing in their number.
55 Finally, they will emit a detectable flux of nonthermal photons via bremsstrahlung.

56 Early observations of long-duration bursts, though limited in number, measured X-ray
57 fluxes in a few keV to a few hundred keV range, or γ -ray fluxes in MeV regions, suggesting
58 that these prolonged emissions are also due to relativistic electrons [*McCarthy and Parks*,
59 1985; *Eack et al.*, 1996, 2000; *Brunetti et al.*, 2000; *Chubenko et al.*, 2000]. Several recent
60 observations [*Tsuchiya et al.*, 2007; *Torii et al.*, 2009; *Tsuchiya et al.*, 2009; *Chilingarian*
61 *et al.*, 2010] have reinforced the suggestion, by detecting photon spectra extending clearly
62 to 10 MeV or higher, and have given evidence that those long-duration γ rays are also
63 produced via bremsstrahlung. These results naturally lead to a view that long-duration
64 events are also caused by relativistic runaway electrons. However, compared with short-
65 duration ones, the nature of long-duration bursts have remained less understood, due
66 primary to the lack of a sufficiently large sample. For example, it is still unclear how the

67 electron acceleration process keeps operating for such long durations. In addition, the
68 relation between short-duration bursts and long-duration ones is unknown.

69 Aiming at detections of radiation bursts from thunderstorm activity, we have been op-
70 erating the Gamma-Ray Observations of Winter THunderclouds (GROWTH) experiment
71 since 2006 December 20. In this paper, we report on successful GROWTH detections
72 of two long-duration γ -ray bursts extending to 10 MeV. Using the acquired γ -ray data,
73 the source distance, its spatial extent, and the number of relativistic electrons involved
74 therein are estimated. Then, a γ -ray spectrum which sums up 3 GROWTH detections is
75 compared with cumulative TGF spectra obtained by two independent space observations.
76 Based on these results, we quantitatively discuss the production mechanism of prolonged
77 γ -ray bursts from winter thunderclouds.

2. The GROWTH Experiment

78 The GROWTH experiment, comprising two independent subsystems, has been oper-
79 ating successfully at a roof of a building of Kashiwazaki-Kariwa nuclear power plant in
80 Niigata Prefecture, Japan. Figure 1 shows the location of the plant, facing the Japan Sea,
81 and the GROWTH experimental site therein. The geographical longitude, latitude, and
82 altitude of the experimental site are $138^{\circ}36'E$, $37^{\circ}26'N$, and 40 m above sea level, respec-
83 tively. This coastal area is frequently struck by strong thunderstorms in winter seasons.
84 Actually, before the GROWTH experiment started working, radiation monitors (filled
85 circles in Fig. 1), which are arranged at around 300 m – 400 m intervals in the plant,
86 occasionally observed > 3 MeV intense radiation enhancements in winter seasons, which
87 are difficult to ascribe to so-called radon washouts because these rainfall-related episodes
88 would mainly cause increases at < 3 MeV energies [e.g. *Yoshioka, 1992; Yamazaki et al.*,

2002]. Each radiation monitor consists of a $\phi 5.1 \text{ cm} \times 5.1 \text{ cm}$ NaI (Tl) scintillation counter,
and a spherical ion chamber with a volume of $\sim 14 \text{ L}$ that contains Ar gas. The former
covers the $50 \text{ keV} - 3 \text{ MeV}$ energy range, while the later operates in $> 50 \text{ keV}$. However,
the radiation monitors have too poor a time resolution of 30 sec, together with the too
limited energy bands, to understand the nature of those phenomena. The GROWTH
experiment is expected to provide much improved knowledge on these sporadic events.

The pictures and drawings of the two subsystems are given in *Enoto et al.* [2007] and
Tsuchiya et al. [2007]. One of them (Detector-A) uses two cylindrical NaI (Tl) scin-
tillators (density = 3.67 gcm^{-3}), having a diameter and a height of both 7.62 cm. In
order to actively shield them from natural low-energy ($< 3 \text{ MeV}$) environmental radiation
(e.g. from ^{40}K), the NaI scintillators are individually surrounded by well-shaped BGO
($\text{Bi}_4\text{Ge}_3\text{O}_{12}$; density = 7.1 gcm^{-3}) scintillators, with the thickness on the side and bottom
being 1.27 cm and 2.54 cm, respectively. The BGO scintillators geometrically shield the
central NaI up to a solid angle of 2.4π str, or $0.6 \times 4\pi$. Thus, the NaI scintillators have
a higher sensitivity toward the sky direction. The two central NaI scintillators and the
BGO shields are operated over an energy range of $40 \text{ keV} - 10 \text{ MeV}$. Output signals from
photomultiplier tubes, attached to the NaI and BGO, are fed individually to a 12 bit 8ch
VME-analog-to-digital converter [ADC (CP 1113A)] with a time resolution of $10 \mu\text{sec}$,
and is recorded on event-by-event basis.

As another feature of Detector-A, a 0.5 cm thick plastic scintillator with an area of
 $30.5 \text{ cm} \times 15.2 \text{ cm} = 464 \text{ cm}^2$ is placed above the two NaI scintillators, and operated with
a threshold energy of $> 1 \text{ MeV}$. It has a high detection efficiency for charged particles,
while it is almost transparent to photons due to its thinness and higher threshold. Utiliz-

112 ing this feature, we can separate charged particles from photons, and efficiently exclude
113 background cosmic-ray muons, which typically deposit > 1 MeV energies, from events in
114 the two NaI scintillators. Specifically, an event in either of the two NaI scintillators is
115 judged as a charged particle if it give a simultaneous hit (with 10μ sec) in the plastic
116 scintillator. Thus, utilizing signals of the BGO and plastic scintillators both in anticoin-
117 cidence, the central NaI scintillators effectively detect photons, generally arriving from a
118 sky direction.

119 Aiming at an independent radiation measurement, another subsystem (Detector-B) was
120 installed ~ 10 m apart from Detector-A. It consists of spherical NaI (Tl) and CsI (Tl)
121 scintillators (density = 4.51 gcm^{-3}), both with a diameter of 7.62 cm. The former op-
122 erates in 40 keV –10 MeV, while the latter covers a higher energy μ range of 300 keV –
123 80 MeV. Unlike Detector-A, these scintillators have omni-directional sensitivity because
124 they have no shields such as the BGO or plastic scintillators. Output signals of two pho-
125 tomultiplier tubes, attached to the NaI and CsI crystals, are sampled by a self-triggering
126 electronics system with a 12 bit ADC (AD 574). These events are accumulated into an
127 ADC histogram, which is recorded every 6 sec.

128 Energy calibrations of Detector-A and Detector-B were carried out, using natural envi-
129 ronmental γ -ray lines of ^{214}Pb (0.352 MeV), ^{214}Bi (0.609 MeV), ^{40}K (1.46 MeV), and ^{208}Tl
130 (2.61 MeV). Then, especially for the CsI of Detector-B, cosmic-ray muons, giving energy
131 deposits with its peak of around 35 MeV, were also utilized. Basically, these calibrations
132 are performed and checked by an offline analysis.

133 In addition to those radiation detectors, the GROWTH system utilizes three optical
134 sensors and an electric-field mill as environmental monitors. Each optical sensor consists

135 of a hand-made analog circuit, and a silicon photodiode (HAMAMATSU S1226-8BK)
136 which is sensitive over a wavelength range of 320 nm – 1000 nm (with its peak at 750
137 nm). They measure environmental visible light in coarsely different directions; sea side,
138 zenith direction, and anti-sea side. The output signals are fed to a 12 bit VME-ADC, and
139 recorded every 0.1 sec. The electric field mill is a commercial product (BOLTEK EFM-
140 100). Its analog output is fed to a 12 bit ADC (AD 7892), and recored as electric-field
141 strength between $\pm 100 \text{ kV m}^{-1}$, with a resolution of 50 Vm^{-1} .

3. Results

3.1. Count histories of the inorganic scintillators

142 Figure 2 shows count histories of the 4 inorganic scintillators of Detector-A and B,
143 obtained over 15:00 – 17:00 UT on 2007 December 13 which corresponds to local midnight
144 (0:00 – 2:00 JST on 2007 December 14). For reference, typical background rates per 20
145 sec, corresponding to the panels (a), (b), (c), and (d) of Fig. 2, are 22000, 1700, 2100, and
146 1500, respectively. Similarly, Figure 3 gives those over 8:30 – 10:30 UT on 2008 December
147 25 (17:30 – 19:30 JST on the same day, or local evening). On both these days, a strong
148 low pressure system (with $\sim 990 \text{ hPa}$ on the ground) developed over Japan, causing
149 thunderstorms at the coastal area of Japan Sea. A gradual count increase, followed by a
150 gradual count decrease, generally shows that they are due mainly to radioactive radon and
151 its decay products in rain, with their half-lives being 20 – 30 min. These effects originating
152 from radionuclides are closely investigated by *Suszcynsky et al.* [1996] and *Yamazaki et al.*
153 [2002].

154 Superimposed on such gradual count increases, a sharp count enhancement is found in all
155 the inorganic scintillators at around 16:00 UT in Fig. 2, and at around 9:30 UT in Fig. 3.

156 Hereafter, we call the former and the latter events 071213 and 081225, respectively. These
157 enhancements, both lasting for 70 – 80 sec, are quite different from the radon effects and
158 from short radiation bursts associated with lightning discharges. Among those inorganic
159 scintillators, BGO of Detector-A gave statistically the most significant burst detection on
160 both occasions; 30σ for 071213 and 19σ for 081225. This is because it has a higher density
161 and a larger effective atomic number, and hence a higher stopping power, especially for
162 X/ γ rays, than the other inorganic scintillators used in our system.

163 Figure 4 shows NaI count histories of 071213 in 3 energy bands from Detector-A and
164 B, while Figure 5 represents those of 081225. For comparison with Detector-B, the data
165 of Detector-A [panels (a), (b) and (c) of Fig. 4 and Fig. 5] are presented without the
166 BGO or plastic anticoincidence. With a criterion that both the NaI and CsI scintillators
167 of Detector-B simultaneously record 10 or higher counts per 12 sec in the 3 – 10 MeV
168 energy band, we define burst periods of 071213 and 081225 as 84 sec, 15:59:29 – 16:00:53
169 UT, and 72 sec, 9:28:29 – 9:29:37 UT, respectively. For reference, this energy band of
170 either scintillator typically records $\sim 4 - 5$ events per 12 sec in quiescent periods; so the
171 above criterion (again, not either but both scintillators have 10 or higher counts) means
172 approximately $\geq 3.2 - 4.0\sigma$ above the background.

173 In order to estimate background levels of individual energy bands of Detector-A and B,
174 we excluded data over the burst period (as defined above) and the adjacent 12-sec periods.
175 The remaining data in the two lower-energy bands were fitted by a quadratic function
176 (via χ^2 evaluation), while those in the highest-energy band with a constant. Table 1
177 summarizes the net count increases, obtained by subtracting interpolated background
178 (dashed curves of Fig. 4 and Fig. 5) from the total counts in the burst period. Thus,

179 the burst detection is statistically significant in each of the three energy bands on both
180 occasions. Table 1 also gives the observed photon number fluxes above the detectors
181 using power-law spectra obtained later (Sec.3.5) and the detector responses of Detector
182 B derived from a Monte Carlo simulation based on GEANT4 [Agostinelli et al., 2003].
183 Here, the MC simulation was evaluated with radionuclide sources of ^{60}Co and ^{137}Cs .

3.2. Arrival directions

184 Shown in Fig. 4 and Fig. 5 are the NaI count rates of Detector A at > 3 MeV energies
185 of 071213 and 081225, respectively, with [panel (d) in both figures] and without [panel
186 (c)] anticoincidence. In both figures, the anticoincidence, which utilizes BGO and plastic
187 signals in logical "OR", is seen to reduce the NaI background level (solid curves) to
188 ~ 0.05 times that without anticoincidence. In contrast, the NaI-detected burst signal rate
189 decreases due to the anticoincidence only to 0.25 ± 0.03 and 0.31 ± 0.06 times the raw rates,
190 for 071213 and 081225, respectively. Thus, the burst photons survive the anti-coincidence
191 with 5 – 6 times higher efficiency than the background events. Similarly, the ratio of the
192 > 40 keV NaI [Fig. 2 (b) and Fig. 3 (b)] to the > 40 keV BGO count rates [Fig. 2 (a) and
193 Fig. 3 (a)], which is normally ~ 0.08 due mostly to environmental radioactivity coming
194 from omni-directions, increased to 0.18 ± 0.02 for 071213 and 0.14 ± 0.02 for 081225.

195 The above properties revealed by applying the anticoincidence are thought to reflect
196 arrival directions of the burst signals. If they came mainly from horizontal or ground
197 directions, the anticoincidence on/off ratio and the NaI/BGO ratio would both fall below
198 their normal values, because, e.g., 40 keV or 3 MeV γ rays horizontally entering Detector-
199 A would be almost fully or partially (at least 30%) absorbed/scattered by BGO via
200 photoelectric absorption and Compton scattering. Accordingly, we conclude that the

burst signals arrived from sky directions, not from horizontal or ground directions. A more quantitative study of arrival directions, employing Monte Carlo simulations, will be reported elsewhere.

3.3. Burst components

Figure 6 shows count histories of the plastic scintillator (> 1 MeV) and the environmental sensors. In coincidence with the apparent signals detected by the inorganic scintillators, the 0.5 cm thick plastic scintillator gave count increases in individual burst periods by $N_{\text{pl}} = 160 \pm 30$ (5.3σ) for 071213 and 72 ± 18 (4σ) for 081225 [top panels of Fig. 6]. Presumably these plastic signals are composed of γ rays and charged particles, most likely electrons, which are either accelerated primaries or secondary ones produced by high-energy photons via Compton scattering. Below, we estimate how γ rays and electrons contribute to N_{pl} , and estimate the electron flux above 1 MeV.

First, a Monte Carlo simulation using GEANT4 predicts that the plastic scintillator has a low detection efficiency, 0.5 – 1%, for > 1 MeV γ rays, while that for > 1 MeV electrons reaches 75 – 90%. Next, using power-law spectra obtained later (Sec.3.5) and the effective area of the NaI scintillator of Detector B yield 1 – 10 MeV photon number fluxes above the GROWTH system as $(17.9 \pm 1.8) \times 10^{-2} \text{ cm}^{-2}\text{s}^{-1}$ for 071213, and $(9.2 \pm 1.8) \times 10^{-2} \text{ cm}^{-2}\text{s}^{-1}$ for 081213. Then, multiplying these fluxes by the GEANT4-derived detection efficiency for γ rays of the plastic scintillator and the area of the plastic scintillator, 464 cm^2 , γ -ray produced counts contributing to N_{pl} are estimated as $N_{\gamma} = 70 \pm 7$ for 071213, and 31 ± 6 for 081225. Finally, subtracting N_{γ} from N_{pl} , the contribution of electrons is obtained as 90 ± 30 for 071213, and 41 ± 19 for 081225. Although these numbers, when taken at their face values, imply a significant electron contribution to N_{pl} , here we conservatively regard

223 them as upper limits. Then, a 95% confidence level upper limit on the electron flux above
224 1 MeV of 071213 and 081225 is computed as $0.5 \times 10^{-2} \text{ cm}^{-2}\text{s}^{-1}$ and $0.3 \times 10^{-2} \text{ cm}^{-2}\text{s}^{-1}$,
225 respectively. These upper limits are more than an order of magnitude lower than the
226 1 – 10 MeV γ -ray fluxes. Therefore, the observed burst signals arriving at the GROWTH
227 system are inferred to be dominated by photons, rather than electrons.

3.4. Comparison with signals from environmental sensors

228 The visible-light sensor (middle panels of Fig. 6) recorded an extremely intense signal,
229 lasting ≤ 1 sec, at 15:57:50 UT and 9:25:09 UT, for 071213 and 081225, respectively. In
230 coincidence with the recorded optical flashes, the electric field rapidly changed its polarity
231 from positive to negative (bottom panels of Fig. 6). These indicate that a lightning
232 discharge occurred. However, their occurrence is well separated from the γ -ray bursts
233 themselves, namely, 100 sec and 180 sec prior to the 071213 and 082125 commencements,
234 respectively. Thus, we conclude that neither of the present two γ -ray bursts coincided
235 with lightning discharges.

236 Prior to the present work, *Tsuchiya et al.* [2007, 2009] have reported similar lack of
237 coincidence between prolonged γ -ray bursts and lightning discharges. In *Tsuchiya et al.*
238 [2007], a long-duration burst, lasting 40 sec, was detected by the GROWHT system 70 sec
239 prior to lightning, while in *Tsuchiya et al.* [2009], no lightning discharges were measured
240 over 5 minutes before or after a prolonged (~ 90 sec) burst detected at a high-mountain
241 detector. These previously reported events, observed during thunderstorms, have also
242 been considered to be associated with thunderclouds.

243 In the same manner, we associate the present bursts with the thunderclouds, rather
244 than to lightning discharges. Actually, rainfall-thunder observation data¹, provided by

245 a laser observation system operated by Tokyo Electric Power Company, showed that
246 thunderclouds approached the Kashiwazaki-Kariwa nuclear plant from the sea side on
247 both occasions, and passed over it during the 10 minutes.

3.5. Energy spectra

248 Figure 7 and Figure 8 show background-subtracted GROWTH spectra, obtained in the
249 burst periods of 071213 and 081225, respectively. In either case, we accumulated the data
250 over the burst period, and subtracted background spectra which were averaged over 10
251 minutes before and after the burst, although thunderstorms were ongoing during these
252 time periods. This is to remove < 3 MeV line- γ rays induced mainly by radon decays,
253 which increase the background level by up to twice. To examine how the background
254 selection affects the final spectra (Figure 7 and Figure 8), we subtracted an alternative
255 background spectrum averaged over 5 minutes before and after the burst. However, the
256 background-subtracted spectra did not change by more than $\pm 10\%$ at < 1 MeV, or $\pm 5\%$
257 at > 1 MeV. These are almost negligible compared with the statistical errors.

258 In both events, the background-subtracted spectra of Detector-A and Detector-B exhibit
259 very hard continuum spectra, which clearly extend to 10 MeV. As shown in another
260 GROWTH event 070106 reported previously [*Tsuchiya et al.*, 2007], and in high-mountain
261 observations [*Torii et al.*, 2009; *Tsuchiya et al.*, 2009; *Chilingarian et al.*, 2010], similar
262 prolonged γ -ray emissions, extending to 10 MeV or higher, were observed, and have been
263 thought to be produced via bremsstrahlung. Thus, the present high-energy γ rays must
264 also be produced via bremsstrahlung by electrons accelerated beyond 10 MeV. Given these
265 results, the present two events, together with the previous ones, may be understood as
266 manifestations of a common type of high-energy activity in thunderstorms.

As easily seen in Fig. 7 and Fig. 8, the obtained spectra, in particular those of Detector-
 B, flatten in 0.8 – 3 MeV, even though they are not corrected for the detector responses.
 One of the causes of this flat is the Compton scattering: since the Compton scattering cross
 section in the atmosphere increases as photon energy decreases toward 0.1 MeV, photons
 at low energies would experience stronger Compton degradation than higher-energy ones.

3.6. Model fits

Supposing that the burst γ rays were produced in a source located at a certain distance and propagated through atmosphere to reach our detectors, we may deduce the initial photon spectrum at the source, and estimate the source distance, from the background-subtracted spectra. Since the Detector-A spectra are complicated due to the passive and active shielding effects by the BGO well, below we analyze the Detector-B spectra. According to numerical calculations [*Roussel-Dupré et al.*, 1994; *Roussel-Dupré and Gurevich*, 1996; *Lehtinen et al.*, 1999; *Babich et al.*, 2007], an energy distribution function of runaway electrons, generated under the RREA mechanism, is expressed by a power-law function, or more precisely, an exponentially cut-off power-law. Consequently, we assume an initial photon number spectrum as

$$f(\epsilon_p) = \alpha \epsilon_p^{-\beta} \exp(-\epsilon_p/\epsilon_c) \text{ (MeV}^{-1}\text{sr}^{-1}\text{)}. \quad (1)$$

Here, α and β are a normalization factor and a photon index, respectively, while ϵ_p and ϵ_c describe the emitted photon energy and a cut-off energy in MeV, respectively. While this equation represents an exponentially cut-off power law, it can also express a pure power-law by requiring $\epsilon_c \rightarrow \infty$.

276 Below, let us estimate the source distance d from our Detector-B data, as well as α ,
277 β , and ϵ_c . In order to simulate the photon propagation in the atmosphere, we utilize
278 EGS4 [Nelson et al., 1985] embedded in CORSIKA 6.500 [Heck et al., 1998]. In the
279 CORSIKA simulation, the atmosphere consists of N₂, O₂, and Ar with the mole ratios
280 of 78.1%, 21.0%, and 0.9%, respectively. The density of the atmosphere, divided into 5
281 layers, depends exponentially on the altitude h , with a form of $A + B \exp(-h/C)$, with
282 A, B, C being model parameters. For example, at $h < 4$ km, the model is specified as
283 $A = -186.6 \text{ g cm}^{-2}$, $B = 1222.7 \text{ g cm}^{-2}$, and $C = 9.94 \text{ km}$ [Heck and Pierog, 2009].
284 In addition, EGS4 can adequately treat electromagnetic processes in the relevant energy
285 range of a few tens of keV to a few tens of MeV.

286 Mono-energetic photon simulations were carried out for 33 incident energies from 50
287 keV to 100 MeV. The energy interval is set to 10 keV for 50 keV – 90 keV, 100 keV for
288 100 keV – 1 MeV, 1 MeV for 1 MeV – 10 MeV, and 10 MeV for 10 MeV – 100 MeV.
289 For one mono-energetic photon simulation, one million photons were vertically injected
290 to the atmosphere from a fixed source distance. In reality, 20 source distances from 20 m
291 to 2000 m were applied for one mono-energetic simulation. Then, we saved the energy,
292 angle, and species of all of photons and particles that arrive at the observatory level (40
293 m above sea level).

294 Figure 9 indicates three representative sets of simulated photon spectra, propagating
295 over $d = 300 \text{ m}$ (36 g cm^{-2}), 1000 m (120 g cm^{-2}), and 2000 m (220 g cm^{-2}), with the
296 numbers in parentheses giving air mass calculated by the above exponential formula.
297 Punch-through photons, which suffer no interactions with air molecules, appear as a
298 strong peak at the highest end of each photon spectrum, while scattered ones form a

continuum toward lower energies. As the distance increases, the punch-through photons
and the scattered continuum are both strongly attenuated, in particular toward lower
energies, due primarily to Compton scattering. For instance, the survival probability for
10 (1) MeV punch-through photons to propagate over $d = 2000$ m is only 0.02 (10^{-5})
times that over $d = 300$ m. Note that as discussed later in Sec. 4.3, a long-duration
burst probably changes in the burst period its viewing angle relative to a beam axis of
electrons accelerated in thunderclouds. Thus, the calculated photon spectra here would
vary according to the changes, and hence they will be treated in this work as ones averaged
over different viewing angles.

Convolving the simulated photon spectra with the detector responses, we can obtain
a model-predicted spectrum to be observed by the NaI and CsI scintillators. Finally,
we convolve these model predictions with the assumed source photon spectrum, eq.(1),
and fit the predictions simultaneously to the background-subtracted NaI and CsI spectra
(right panels of Fig. 7 and Fig. 8). Then, the model parameters, such as α , β and ϵ_c , can
be determined so as to minimize the fit χ^2 .

Shown in Figure 10 are three representative model fits to the spectra of 071213 and
081225, assuming a power-law model. The choice of d of 300, 1000, and 2000 m in
Fig. 10, respectively gave χ^2 values as 48.4, 77.5, and 116 for 071213, and 40.9, 46.7, and
51.4 for 081225. By changing d and repeating the fitting, we obtained χ^2 curves as shown
in Figure 11, together with the χ^2 minima as 46.5 at $d = 400$ m for 071213, and 40.9 at
 $d = 300$ m for 081225. From these figure, we can constrain source distance. Table 2 and
Table 3 summarize the best-fit parameters for 071213 and 081225, respectively, together
with the constrained source distance. Also, low-energy parts (< 300 keV) of the two

322 spectra are found to play an important role to determine d . If we use the background
323 averaged over the 5 min intervals (instead of 10 min), the source distances become 350 m
324 for 071213, and 300 m for 081225. Thus, the distance is not affected significantly by the
325 systematic background uncertainty.

326 The NaI and CsI spectra have been explained, in either event, by a common set of model
327 parameters, although the fits are not necessarily good enough. The cut-off energy E_c was
328 constrained to be rather high with relatively large errors. Thus, our data do not provide
329 evidence for spectral cut-off in either event. In agreement with this, the two spectral
330 models, a power law and an exponentially cut-off power law, gave similar goodness of fits
331 in both events. Importantly, the source distance have been constrained with a reasonable
332 accuracy.

333 As another attempt, we tentatively fixed E_c at 7 MeV, which is the expected average
334 kinetic energy of runaway electrons (not of bremsstrahlung photons), and repeated the
335 model fitting. Then, the fit became worse in both events (4th column of Table 2 and
336 Table 3). Therefore, the initial photon spectrum is again inferred to extend beyond ~ 7
337 MeV.

4. Discussion

4.1. Source heights

338 Assuming a power-law function at the source, the γ -ray spectra of 071213 and 081225
339 suggest that the sources are located at 290 – 560 m ($35 - 67 \text{ g cm}^{-2}$) and 120 – 690 m
340 ($14 - 82 \text{ g cm}^{-2}$) above our system, respectively, both at 90% confidence level. In fact,
341 these constraints are in good agreement with the known heights of winter thunderclouds in
342 this area. Winter thunderclouds and winter lighting observed at the coastal area of Japan

343 Sea exhibit many features that have hardly been found from those in summer seasons
344 and/or in other areas (e.g. *Rakov and Uman* [2005] and references therein). These include
345 rather low altitudes of the development of these thunderclouds. Actually, *Goto and Narita*
346 [1992] conducted video observations of winter lightning at the same Niigata Prefecture
347 as our experimental site, and reported that the visible bases of winter thunderclouds are
348 typically located at 200 m – 800 m above sea level. Also, a recent numerical calculation
349 done by *Babich et al.* [2010] shows that another GROWTH event [*Tsuchiya et al.*, 2007]
350 may be produced at a source height of 0.5 – 2 km, and hence generally agrees with the
351 present results.

352 These height estimations provide an additional clue to the possible electron contribu-
353 tions to the detected plastic signals (Sec. 3.3). As argued so far, electrons are considered
354 to be accelerated in these thunderclouds to at least 10 MeV, probably a few tens of MeV.
355 Since such electrons have a range of < 100 m at near the sea level, they would hardly reach
356 our system, even if a range straggling is taken into account. Therefore, it is reasonable
357 that the electron flux incident on our system, if any, was much lower than that of photons.

358 Unlike the present sea-level observations, some high-mountain experiments, conducted
359 at Mt. Norikura (2770 m) in Japan [*Tsuchiya et al.*, 2009] and Mt. Aragatz (3250 m)
360 in Armenia [*Chilingarian et al.*, 2010], have detected primary electrons in long duration
361 events (numbers in parentheses indicate altitudes of observatories). *Tsuchiya et al.* [2009]
362 estimated the source height as 60 – 130 m (90% confidence level), while *Chilingarian et al.*
363 [2010] evaluated it as 100 – 150 m. These low source heights, which are comparable to or
364 shorter than the expected electron range, can naturally explain their electron detections.

4.2. Extent and motion of the γ -ray beams

365 Measuring electric-field structure of winter thunderclouds, *Kitagawa and Michimoto*
366 [1994] revealed that tripole electrical structures, which consist of positive, negative and
367 positive layers from top to bottom, appear at mature stages of winter thunderclouds.
368 Then, they observed the tripole structures to last for < 10 minutes in early or late winter,
369 while less than several minutes in midwinter. Since the present two events were observed
370 in midwinter, the measured burst periods of 84 sec of 071213 and 72 sec of 081225 are
371 consistent with their observations, if the burst durations represent the lifetime of electric
372 fields.

373 Figure 12 shows dose variations on 2007 December 13, measured by the nearest and the
374 second nearest radiation monitors of the power plant (5 and 6 in Fig. 1, black and red lines
375 in Fig. 12, respectively). The two monitors gave moderate dose increases for ~ 1 minute
376 or less around the GROWTH event. By examining the GROWTH data of 071213 burst
377 (crosses in Fig. 12), as well as dose rates of the second nearest monitor (red line) obtained
378 for 15:59:30 – 16:01:00 UT and that of the nearest one (black line) obtained over 16:00:00
379 – 16:01:30 UT, peak times of their enhancement can be evaluated as 15:59:48 (± 6 sec)
380 UT, 15:59:58 (± 15 sec) UT, and 16:00:27 (± 15 sec) UT. Thus, referring to the GROWTH
381 data, the second nearest monitor increased in its dose rates with a small delay of 10 ± 16
382 sec (or almost simultaneously), while the nearest one with a larger delay by 39 ± 16 sec.
383 The two monitors are located at a distance of 500 – 600 m from the GROWTH system.
384 For reference, data of the other two radiation monitors (4 and 7 in Fig. 1) exhibited no
385 apparent increases (green and blue lines in Fig. 12). As for 081225, data of those radiation
386 monitors were unavailable due to some data-storage problem.

387 These simultaneous and delayed detections by the two radiation monitors have two
388 important implications. One is that the γ -ray emission from thunderclouds is likely to
389 have illuminated a rather limited area, spreading over ~ 600 m on the ground. This kind
390 of effect was also suggested by five radiation monitors (1–5 in Fig. 1), on the occasion
391 of the other GROWTH event [*Tsuchiya et al.*, 2007], and another experiment conducted
392 on the same coastal area [*Torii et al.*, 2002]. The other is that the γ -ray emitting region
393 moved, presumably together with the thunderclouds.

394 From data of Japan Meteorological Agency, it is found that south-west wind was blowing
395 during 10 minutes including the burst period of 071213. Thus, the south-west direction
396 can naturally explain the delay of the nearest monitor, if the γ -ray emitting region moved
397 together with the thunderclouds. Then, the wind velocity was on average 360 m min^{-1} ,
398 with the maximum of 720 m min^{-1} . Projecting, to south-west axis, the distance between
399 the GROWTH system and the nearest monitor, ~ 500 m, and dividing the projected
400 distance, ~ 350 m, by its delay, 39 ± 16 sec, we obtain an average moving velocity of the
401 emitting region as $540 \pm 220 \text{ m min}^{-1}$. Thus, the estimated moving velocity is generally
402 consistent with the wind velocity.

403 Given above discussions, we may assume that the winter thunderclouds moved from the
404 Japan sea in south-west side to the inland in north-east side. Then, a short-lived tripole
405 structure appeared in a thundercloud, and accelerated ambient fast electrons toward the
406 bottom positive layer. The accelerated electrons emitted γ rays toward the ground, which
407 the GROWTH system and the two radiation monitors detected when the beam passed over
408 them. The differences in the statistical significance of detections between the GROWTH
409 system and the radiation monitors may be due to different positions and effective viewing

410 angles relative to the accelerated electron beam axis in the thundercloud, and to the
 411 differences in their sensitivity. The 081225 event is considered to have occurred under
 412 similar conditions, because west winds, with almost the same velocity as in the 071213
 413 case, were blowing at that time. However, it is presently unclear whether the γ -ray
 414 emission ceased when the tripole structure disappeared, or when the γ -ray beam moved
 415 away from the GRWOTH system as the thunderclouds moved.

4.3. The number of relativistic electrons in thunderclouds

Using the initial photon energy spectrum $f(\epsilon_p)$ of Eq. (1) as quantified in Table 2 and Table 3, we can estimate the number of relativistic electrons radiating the observed 1 – 10 MeV γ rays via bremsstrahlung, as

$$N_e \sim \frac{2\pi}{H} \int_1^{10} dK_e \int_1^{K_e} d\epsilon_p \int_0^{\theta_{\max}} \frac{f(\epsilon_p)}{\eta(K_e, \epsilon_p, \theta)} \sin \theta d\theta. \quad (2)$$

416 Here, $\eta(K_e, \epsilon_p, \theta)$ is the probability per 1 g cm⁻² with which an electron with a kinetic
 417 energy K_e emits a bremsstrahlung photon with an energy ϵ_p at an angle θ with respect
 418 to the electron-beam axis [*Koch and Motz*, 1959], and H denotes the vertical length of
 419 the acceleration region. Since this H is unavailable from the present observations like in
 420 *Tsuchiya et al.* [2009], we assume either $H = 300$ m or 1000 m, corresponding to 35 g cm⁻²
 421 and 110 g cm⁻², respectively. These assumptions are based on intracloud observations of
 422 X rays using a balloon-born detector, which showed that a high electric field region, to
 423 produce a significant flux in 3 – 120 keV energy range, has a vertical extent of ~ 500 m,
 424 at altitudes of 3.7 – 4.2 km [*Eack et al.*, 1996].

425 We further assumed that the electric-field strength in the acceleration region is 300
 426 kV m⁻¹, which is slightly higher than the threshold (at 1 atm) to cause the runaway elec-

427 tron avalanches. When 1 MeV electrons are accelerated from the top of this acceleration
 428 region to the bottom, they will gain energies of 15 MeV for $H = 300$ m, and 19 MeV for
 429 $H = 1000$ m. Therefore, the assumed electric-field strength, together with the assumed
 430 vertical length, is sufficient to produce 10 MeV photons via bremsstrahlung.

431 To calculate eg.(2), we further need to specify θ ; this is suggested to be relatively small,
 432 from the obtained photon spectra. In practice, the angle of prolonged γ -ray event may
 433 vary according to the motion of thunderclouds. Thus, we adopt 15° or 30° as θ_{\max} . As
 434 listed in Table 4, these assumptions, together with eq. (1), give $N_e = 10^9 - 10^{11}$. Similar
 435 estimations for other long-duration γ -ray bursts have given $N_e = 10^8 - 10^{12}$ [*Tsuchiya*
 436 *et al.*, 2007, 2009; *Chilingarian et al.*, 2010]. Thus, long-duration γ -ray bursts appear to
 437 be emitted by a similar number of relativistic electrons.

4.4. Relation between the bursts and the RREA mechanism

A possible source of energetic seed electrons to cause the RREA can be attributable to secondary cosmic rays [*Gurevich et al.*, 1992]. The cosmic-ray flux above 1 MeV, at the presently relevant altitudes of <1 km, is $I_0 \sim 200 \text{ m}^{-2}\text{s}^{-1}$ [*Grieder*, 2001]. Considering the measured burst periods of 70 – 80 sec and the 30 – 40 sec delay of one radiation monitor from the 071213 event, we presume that the acceleration region has a horizontal length of $L \sim 600$ m at most, as judged from the extent of the γ -ray beam of 071213. Possibly, an actual extent of the acceleration region in thunderclouds would be shorter than this 600 m, because the γ -ray beam would diverge due to multiple scatterings of the emitting electrons and Compton scatterings of the emitted γ rays. We may also consider that an acceleration region is sustained in thunderclouds at least for 100 sec. Accordingly, the

number of cosmic rays S_0 , entering the acceleration region, is described as

$$S_0 = 7.2 \times 10^9 \times (L/600 \text{ m})^2 \times \Delta t/100 \text{ sec.} \quad (3)$$

Based on the RREA mechanism, the total number of relativistic electrons at the end of an acceleration region, N_{RREA} , is estimated as

$$N_{\text{RREA}} = S_0 \exp(\delta), \quad \delta = \int_0^H \frac{dz}{\lambda}. \quad (4)$$

The length parameter λ is given as

$$\lambda = \frac{7300 \text{ kV}}{E - (276 \text{ kV m}^{-1})n} \text{ m}, \quad (5)$$

where E is the electric-field strength in kV m^{-1} and n denotes the air density relative to that at 1 atm. This formula is valid for $300 - 3000 \text{ kV m}^{-1}$ [Dwyer, 2003]. Assuming $E = 300 \text{ kV m}^{-1}$ gives $\lambda \sim 300 \text{ m}$ at $P = 1 \text{ atm}$. In practice, E may be somewhat lower than 300 kV m^{-1} , because P during thunderstorms would be usually lower than 1 atm due to lower pressure system, and hence gives $n < 1$. Since a uniform field, $\delta = H/\lambda$, gives $N_{\text{RREA}} = S_0 \exp(H/\lambda)$, the factor $\eta = \exp(H/\lambda)$ is regarded as the avalanche multiplication factor, and becomes 3 and 30 for $H = 300 \text{ m}$ and 1000 m , respectively. As a result, we obtain

$$N_{\text{RREA}} = 2.2 \times 10^{11} \times (L/600 \text{ m})^2 \times \Delta t/100 \text{ sec} \times \eta/30. \quad (6)$$

438 We thus obtain $N_{\text{RREA}} = 10^{10} - 10^{11}$, which agrees generally with the derived $N_e =$
 439 $10^9 - 10^{11}$. Thus, the standard RREA process can explain at least the present two
 440 prolonged bursts.

441 In the above estimation, we assumed an electric field is slightly higher than the RREA
 442 threshold. However, a weaker field below this threshold might suffice to produce prolonged

443 γ -ray emission. In reality, a 30 – 120 keV x-ray flux continuously increased while an
 444 electric field is lower by 30% – 60% than the RREA threshold [Eack *et al.*, 1996]. This
 445 quasi-static moderate-level field might be accomplished by e.g. a charging mechanism of
 446 thunderclouds.

4.5. Comparisons with TGFs

447 The derived N_e (sec.4.4) is more than five orders of magnitude lower than the number of
 448 relativistic electrons expected from TGF observations, e.g. $10^{16} - 10^{17}$ [Dwyer and Smith,
 449 2005]. This huge number of relativistic electrons in TGFs may be generated by relativistic
 450 feedback mechanism, involving positrons and X rays propagating in the opposite direction
 451 to runaway electrons [Dwyer, 2007, 2008]. Since the estimated N_e of the present bursts
 452 is in generally agreement with N_{RREA} expected from the simple RREA mechanism, we
 453 conclude that at least the present two events do not require an intense feedback process.

454 In order to better characterize γ -ray spectra of long-duration events, we stacked count
 455 spectra over three bursts, namely, the present two ones and 070106 [Tsuchiya *et al.*,
 456 2007]. Figure 13 compares the summed GROWTH spectrum with averaged TGF ones
 457 obtained by two independent satellites; one sums 289 events measured by Reuven Ramaty
 458 High Energy Solar Spectroscopic Imager (RHESSI) [Dwyer and Smith, 2005], while the
 459 other averages over 34 events observed by the Astrorivelatore Gamma a Immagini Leggero
 460 (AGILE) satellite [Marisaldi *et al.*, 2010a]. Thus, the composite GROWTH spectrum is
 461 rather similar in shape to those from TGFs, although three spectra all include detector
 462 responses. This resemblance is consistent with our basic standpoint [Tsuchiya *et al.*,
 463 2007, 2009] that the long-duration γ rays are emitted by the same bremsstrahlung process
 464 as TGFs.

465 On a close comparison, the TGF spectra, especially the AGILE one, appear to have
466 a higher cut-off energy than the GROWTH spectrum. This may be attributable to a
467 difference in the electric potential operating in an acceleration region [*Dwyer and Smith,*
468 2005]. Thus, electrons accelerated in a much lower atmospheric density at the production
469 sites of TGFs, 15 – 40 km [*Dwyer and Smith, 2005; Carlson et al., 2007; Østgaard et al.,*
470 2008], would propagate through a longer distance, which gives a higher electric potential,
471 and gain higher energies because of a smaller ionization loss per unit length.

5. Summary

472 The GROWTH experiment observed two long-duration γ -ray emissions from winter
473 thunderstorms on 2007 December 13 and 2008 December 25. The photon spectra ob-
474 tained in both events clearly extends to 10 MeV, and are consistent with a scenario
475 that accelerated electrons produce, via bremsstrahlung, the observed γ rays. Adopting a
476 power-law function as the initial photon spectrum at the source, we have constrained the
477 source distance as 290 – 560 m for 071213 and 110 – 690 m for 081225, both at 90% con-
478 fidence level. These constraints agree with visible-light observations, which show that the
479 bottom of winter thunderclouds is usually located at 200 – 800 m above sea level [*Goto*
480 *and Narita, 1992*]. We have shown a possibility that the observed γ -ray beams move with
481 winter thunderclouds, and spread over ~ 600 m.

482 We estimated the number of relativistic electrons to cause the present prolonged γ -ray
483 emissions as $10^9 - 10^{11}$. These are in general agreement with those expected from the stan-
484 dard RREA mechanism triggered by secondary cosmic rays. The cumulative GROWTH
485 spectrum, summed over the present two ones and another GROWTH event [*Tsuchiya*

486 *et al.*, 2007], was found to be similar in basic spectral features with the averaged TGF
487 spectra [Dwyer and Smith, 2005; Marisaldi *et al.*, 2010a].

488 **Acknowledgments.** We thank members of radiation safety group at Kashiwazaki-
489 Kariwa power station, Tokyo Electric Power Company, for supporting our experiment.
490 This work is supported in part by the Special Research Project for Basic Science at
491 RIKEN, titled “Investigation of Spontaneously Evolving Systems”, and the Special Podoc-
492 toral Research Project for Basic Science at RIKEN. The work is also supported in part
493 by Grant-in-Aid for Scientific Research (S), No.18104004, and Grant-in-Aid for Young
494 Scientists (B), No. 19740167.

Notes

495 1. rainfall-thunder observation data are available from <http://thunder.tepco.co.jp/>

References

- 496 Agostinelli, S., et al., (2003), Geant4a simulation toolkit, *Nucl. Inst. Meth. A* 506, 250,
497 doi:10.1016/S0168-9002(03)01368-8.
- 498 Alexeenko, V. V., N. S. Khaerdinov, A. S. Lidvansky, and V. B. Petkov (2002), Tran-
499 sient variations of secondary cosmic rays due to atmospheric electric field and evidence
500 for pre-lightning particle acceleration, *Phys. Lett. A* 301, 299, doi:10.1016/S0375-
501 9601(02)00981-7.
- 502 Babich, L. P., E. N. Donskoi, R. I. Ilkaev, I. M. Kutsyk, and R. A. Roussel-Dupré (2004),
503 Fundamental parameters of a relativistic runaway electron avalanche in air, *Plasm.*
504 *Phys. Rep.* 30, 616, doi:10.1134/1.1778437.

- 505 Babich, L. P., E. N. Donskoi, I. M. Kutsyk, and R. A. Roussel-Dupré (2005), The
506 feedback mechanism of runaway air breakdown, *Geophys. Res. Lett.* *32*, L09809,
507 doi:10.1029/2004GL021744.
- 508 Babich, L. P., E. N. Donskoy, and R. A. Roussel-Dupré (2007), Study of relativistic
509 electron avalanche enhancement in the atmosphere at low overvoltages due to avalanche
510 bremsstrahlung, *Geomag. and Aeron.* *47*, 515, doi:10.1134/S0016793207040135.
- 511 Babich, L. P., E. I. Bochkov, E. N. Donskoi, and I. M. Kutsyk (2010), Source of prolonged
512 bursts of high-energy gamma rays detected in thunderstorm atmosphere in Japan at
513 the coastal area of the Sea of Japan and on high mountaintop, *J. Geophys. Res.*, *115*,
514 A09317, doi:10.1029/2009JA015017.
- 515 Bell, T. F., V. P. Pasko, and U. S. Inan (1995), Runaway electrons as a source of Red
516 sprites in the mesosphere, *Geophys. Res. Lett.* *22*, 2127, doi:10.1029/95GL02239.
- 517 Briggs, M. S., et al. (2010), First results on terrestrial gamma ray flashes from the Fermi
518 Gammaray Burst Monitor, *J. Geophys. Res.*, *115*, A07323, doi:10.1029/2009JA015242.
- 519 Brunetti, M., S. Cecchini, M. Galli, G. Giovannini, and A. Pagliarin (2000), Gamma-ray
520 bursts of atmospheric origin in the MeV energy range, *Geophys. Res. Lett.* *27*, 1599,
521 doi:10.1029/2000GL003750.
- 522 Carlson, B. E., N. G. Lehtinen, and U. S. Inan (2007), Constraints on terrestrial
523 gamma ray flash production from satellite observation, *Geophys. Res. Lett.* *34*, L08809,
524 doi:10.1029/2006GL029229.
- 525 Chilingarian, A., A. Daryan, K. Arakelyan, A. Hovhannisyan, B. Mailyan, L. Melkumyan,
526 G. Hovsepyan, S. Chilingaryan, A. Reymers, and L. Vanyan (2010), Ground-based
527 observations of thunderstorm-correlated fluxes of high-energy electrons, gamma rays,

- 528 and neutrons, *Phys. Rev. D* *82*, 043009, doi:10.1103/PhysRevD.82.043009.
- 529 Chubenko, A. P. et al. (2000), Intensive X-ray emission bursts during thunderstorms,
530 *Phys. Lett. A* *275*, 90, doi:10.1016/S0375-9601(00)00502-8.
- 531 Chubenko, A. P. et al. (2009), Energy spectrum of lightning gamma emission, *Phys. Lett.*
532 *A* *373*, 2953, doi:10.1016/j.physleta.2009.06.031.
- 533 Connaughton, V. et al. (2010), Associations between Fermi Gamma-ray Burst Monitor
534 terrestrial gamma ray flashes and sferics from the World Wide Lightning Location Net-
535 work, *J. Geophys. Res.* *115*, A12307, doi:10.1029/2010JA015681.
- 536 Dwyer, J. R. (2003), A fundamental limit on electric fields in air, *Geophys. Res. Lett.* *30*,
537 2055, doi:10.1029/2003GL017781.
- 538 Dwyer, J. R. et al. (2003), Energetic radiation produced during rocket-triggered lightning,
539 *Science* *299*, 694, doi:10.1126/science.1078940.
- 540 Dwyer, J. R. et al. (2004a), Measurements of x-ray emission from rocket-triggered light-
541 ning, *Geophys. Res. Lett.* *31*, L05118, doi:10.1029/2003GL018770.
- 542 Dwyer, J. R. et al. (2004b), A ground level gamma-ray burst observed in association with
543 rocket-triggered lightning, *Geophys. Res. Lett.* *31*, L05119, doi:10.1029/2003GL018771.
- 544 Dwyer, J. R. (2004c), Implications of x-ray emission from lightning, *Geophys. Res. Lett.*,
545 *31*, L12102, doi:10.1029/2004GL019795.
- 546 Dwyer, J. R. et al. (2005), X-ray bursts associated with leader steps in cloud-to-ground
547 lightning, *Geophys. Res. Lett.* *32*, L01803, doi:10.1029/2004GL021782.
- 548 Dwyer, J. R., and D. M. Smith (2005), A comparison between Monte Carlo simulations of
549 runaway breakdown and terrestrial gamma-ray flash observations, *Geophys. Res. Lett.*
550 *32*, L22804, doi:10.1029/2005GL023848.

- 551 Dwyer, J. R. (2007), Relativistic breakdown in planetary atmosphere, *Phys. Plasm.* *14*,
552 04290, doi:10.1063/1.2709652.
- 553 Dwyer, J. R. (2008), Source mechanisms of terrestrial gamma-ray flashes, *J. Geophys.*
554 *Res.* *113*, D10103, doi:10.1029/2007JD009248.
- 555 Eack, K. B., W. H. Beasley, R. W. David, T. C. Marshall, and M. Stolzenburg (1996),
556 Initial results from simultaneous observation of X rays and electric fields in a thunder-
557 storms, *J. Geophys. Res.* *D23*, 29637, doi:10.1029/96JD01705.
- 558 Eack, K. B., D. M. Suszcynsky, W. H. Beasley, R. Roussel-Dupre, and E. Symbalisty
559 (2000), Gamma-ray emissions observed in a thunderstorm anvil, *Geophys. Res. Lett.*
560 *27*, 185, doi:10.1029/1999GL010849.
- 561 Enoto, T., H. Tsuchiya, S. Yamada, T. Yuasa, M. Kawaharada, T. Kitaguchi, M.
562 Kokubun, H. Kato, M. Okano, S. Nakamura, and K. Makishima (2007), Detection
563 of gamma-rays from winter thunderclouds along the coast of Japan Sea, *Proc. 30th Int.*
564 *Cosmic Ray. Conf.* .
- 565 Fishman, G. J. et al. (1994), Discovery of intense gamma-ray flashes of atmospheric origin,
566 *Science* *264*, 1313, doi:10.1126/science.264.5163.1313.
- 567 Goto, Y., and K. Narita, (1992), Observations of winter lightning to an isolate tower, *Res.*
568 *Lett. Atmos. Electr.* *12*, 57.
- 569 Grefenstette, B. W., D. M. Smith, B. J. Hazelton, and L. I. Lopez (2009),
570 First RHESSI terrestrial gamma ray flash catalog, *J. Geophys. Res.* *114*, A02314,
571 doi:10.1029/2008JA013721.
- 572 Grieder, P. K. F. (2001), *Cosmic rays at earth* pp. 198–230, Elsevier Science B. V.,
573 Amsterdam.

- 574 Gurevich, A. V., G. M. Milikh, and R. A. Roussel-Dupré (1992), Runaway electron mech-
575 anism of air breakdown and preconditioning during a thunderstorm, *Phys. Lett. A* *165*,
576 463, doi:10.1016/0375-9601(92)90348-P.
- 577 Gurevich, A. V., G. M. Milikh, and J. A. Valdivia (1997), Model of X-ray emission and
578 fast preconditioning during a thunderstorm, *Phys. Lett. A* *231*, 402, doi:10.1016/S0375-
579 9601(97)00354-X.
- 580 Gurevich, A. V., K. P. Zybin, and Yu. V. Medvedev (2007), Runaway breakdown in strong
581 electric field as a source of terrestrial gamma flashes and gamma bursts in lightning
582 leader steps, *Phys. Lett. A* *361*, 119, doi:10.1016/j.physleta.2006.05.063.
- 583 Heck, D. et al., (1998), Report FZKA 6019, Forschungszentrum Karlsruhe.
- 584 Heck, D., and T. Pierog, (2009), Extensive Air Shower Simulation with CORSIKA: A
585 User's Guide, p.114, Forschungszentrum Karlsruhe,
- 586 Howard, J., M. A. Uman, J. R. Dwyer, D. Hill, C. Biagi, Z. Saleh, J. Jerauld, H. K.
587 Rassoul (2008) Co-location of lightning leader x-ray and electric field change sources,
588 *Geophys. Res. Lett.* *35*, L13817, doi:10.1029/2008GL034134.
- 589 Kitagawa, N., and K. Michimoto (1994), Meteorological and electrical aspects of winter
590 thunderclouds, *J. Geophys. Res.* *99*, 10713, doi:10.1029/94JD00288.
- 591 Koch, H. W., and J. W. Motz (1959), Bremsstrahlung cross-section formulas and related
592 data, *Rev. Mod. Phys.* *31*, 920, doi:10.1103/RevModPhys.31.920.
- 593 Lehtinen, N. G., M. Walt, U. S. Inan, T. F. Bell, and V. P. Pasko (1996), γ -ray emission
594 produced by a relativistic beam of runaway electrons accelerated by quasi-electrostatic
595 thundercloud fields, *Geophys. Res. Lett.* *23*, 2645, doi: 10.1029/96GL02573.

- 596 Lehtinen, N. G., T. F. Bell, and U. S. Inan (1999), Monte Carlo simulation of runaway
597 MeV electron breakdown with application to red sprites and terrestrial gamma ray
598 flashes, *J. Geophys. Res.* *104*, 24699, doi:10.1029/1999JA900335.
- 599 Marisaldi, M., et al., (2010a), Detection of terrestrial gamma ray flashes up to 40 MeV
600 by the AGILE satellite, *J. Geophys. Res.* *115*, A00E13, doi:10.1029/2009JA014502.
- 601 Marisaldi, M., et al., (2010b), Gamma-Ray Localization of Terrestrial Gamma-Ray
602 Flashes, *Phys. Rev. Lett.* *105*, 128501, 10.1103/PhysRevLett.105.128501.
- 603 McCarthy, M. P., and G. K. Parks (1985), Further observations of x-rays inside thunder-
604 storms, *Geophys. Res. Lett.* *12*, 393, doi:10.1029/GL012i006p00393.
- 605 Milikh, G., and J. A. Valdivia (1999), Model of gamma ray flashes due to fractal lightning,
606 *Geophys. Res. Lett.* *26*, 525, doi:10.1029/1999GL900001.
- 607 Moore, C. B., K. B. Eack, G. D. Aulich, and W. Rison (2001), Energetic ra-
608 diation associated with lightning stepped-leaders, *Geophys. Res. Lett.* *28*, 2141,
609 doi:10.1029/2001GL013140.
- 610 Muraki, Y. et al. (2004), Effects of atmospheric electric fields on cosmic rays, *Phys. Rev.*
611 *D* *69*, 123010, doi:10.1103/PhysRevD.69.123010.
- 612 Nelson, W. R., H. Hirayama, and D. W. O Rogers, *Report SLAC 265* (1985).
- 613 Østgaard, N., T. Gjesteland, J. Stadsnes, P. H. Connell, and B. Carlson (2008), Pro-
614 duction altitude and time delays of the terrestrial gamma flashes: Revisiting the
615 Burst and Transient Source Experiment spectra, *J. Geophys. Res.* *113*, A02307,
616 doi:10.1029/2007JA012618.
- 617 Rakov, V. A., and M. A. Uman (2005), Winter lightning in Japan in *Lightning Physics*
618 *and Effects*, 3rd ed., pp. 308 - 320., Cambridge Univ. Press.

- 619 Roussel-Dupré, R. A., A. V. Gurevich, T. Tunnell, and G. M. Milikh (1994), Kinetic theory
620 of runaway air breakdown, *Phys. Rev. E* *49*, 2257, doi:10.1103/PhysRevE.49.2257.
- 621 Roussel-Dupré, R. A., and A. V. Gurevich (1996), On runaway breakdown and upward
622 propagating discharges, *J. Geophys. Res.* *101*, 2297, doi:10.1029/95JA03278.
- 623 Roussel-Dupré, R., J. J. Colman, E. Symbalisky, D. Sentman, and V. P. Pasko (2008),
624 Physical Processes Related to Discharges in Planetary Atmospheres, *Space Sci. Rev.* *137*,
625 51, doi:10.1007/s11214-008-9385-5.
- 626 Smith, D. M., L. I. Lopez, R. P. Lin, and C. P. Barrington-Leigh (2005),
627 Terrestrial gamma-ray flashes observed up to 20 MeV, *Science* *307*, 1085,
628 doi:10.1126/science.1107466.
- 629 Suszcynsky, D. M., R., Roussel-Dupré, and C., Shaw (1996), Ground-based search
630 for X rays generated by thunderstorms and lightning, *J. Geophys. Res.* *101*, 23505,
631 doi:10.1029/96JD02134.
- 632 Torii, T., M. Takeishi, and T. Hosono (2002), Observation of gamma-ray dose increase
633 associated with winter thunderstorm and lightning activity, *J. Geophys. Res.* *107*, 4324,
634 doi:10.1029/2001JD000938.
- 635 Torii T., T. Sugita, S. Tanabe, Y. Kimura, M. Kamogawa, K. Yajima, and H. Yasuda
636 (2009), Gradual increase of energetic radiation associated with thunderstorm activity
637 at the top of Mt. Fuji, *Geophys. Res. Lett.* *36*, L13804, doi:10.1029/2008GL037105.
- 638 Tsuchiya, H. et al. (2007), Detection of high-energy gamma rays from winter thunder-
639 clouds, *Phys. Rev. Lett.* *99*, 165002, doi:10.1103/PhysRevLett.99.165002
- 640 Tsuchiya, H. et al. (2009), Observation of an energetic radiation burst from mountain-top
641 thunderclouds, *Phys. Rev. Lett.* *102*, 255003, doi:10.1103/PhysRevLett.102.255003.

642 Yamazaki, K., S. Tonouchi, and T. Hashimoto (2002), Factors associated with the varia-
643 tions in environmental gamma-ray spectra in Kashiwazaki Kariwa area *J. Radio. Nucl.*
644 *Chem.* *252*, 359, doi:10.1023/A:1015734810119

645 Yoshida, S., T. Morimoto, T. Ushio, Z.-I Kawasaki, T. Torii, D. Wang, N. Takagi, and
646 T. Watanabe (2008), High energy photon and electron bursts associated with upward
647 lightning strokes, *Geophys. Res. Lett.* *35*, L10804, doi:10.1029/2007GL032438.

648 Yoshioka, K. (1992), The seasonal variation of rainout activity of short-lived radon daugh-
649 ters, *Rad. Prot. Dosim.* *45*, 395, doi:

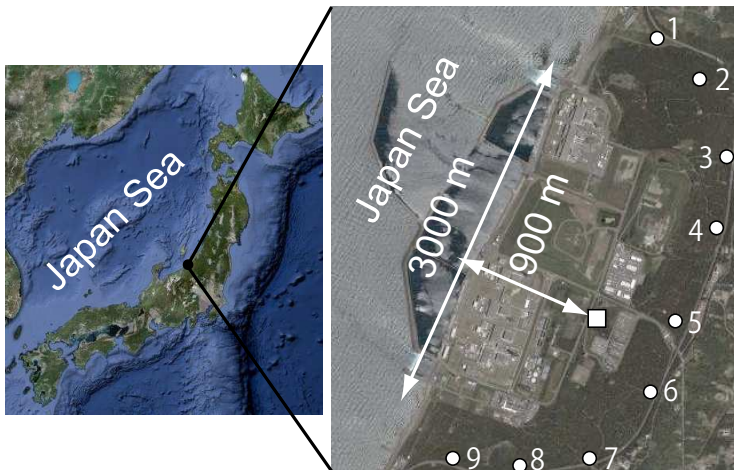


Figure 1. The location of the Kashiwazaki-Kariwa nuclear power plant (left) and its bird view (right). A filled square in the right panel represents the GROWTH experimental site, while 9 filled circles show locations of radiation monitors. Each original image is taken from Google Map.

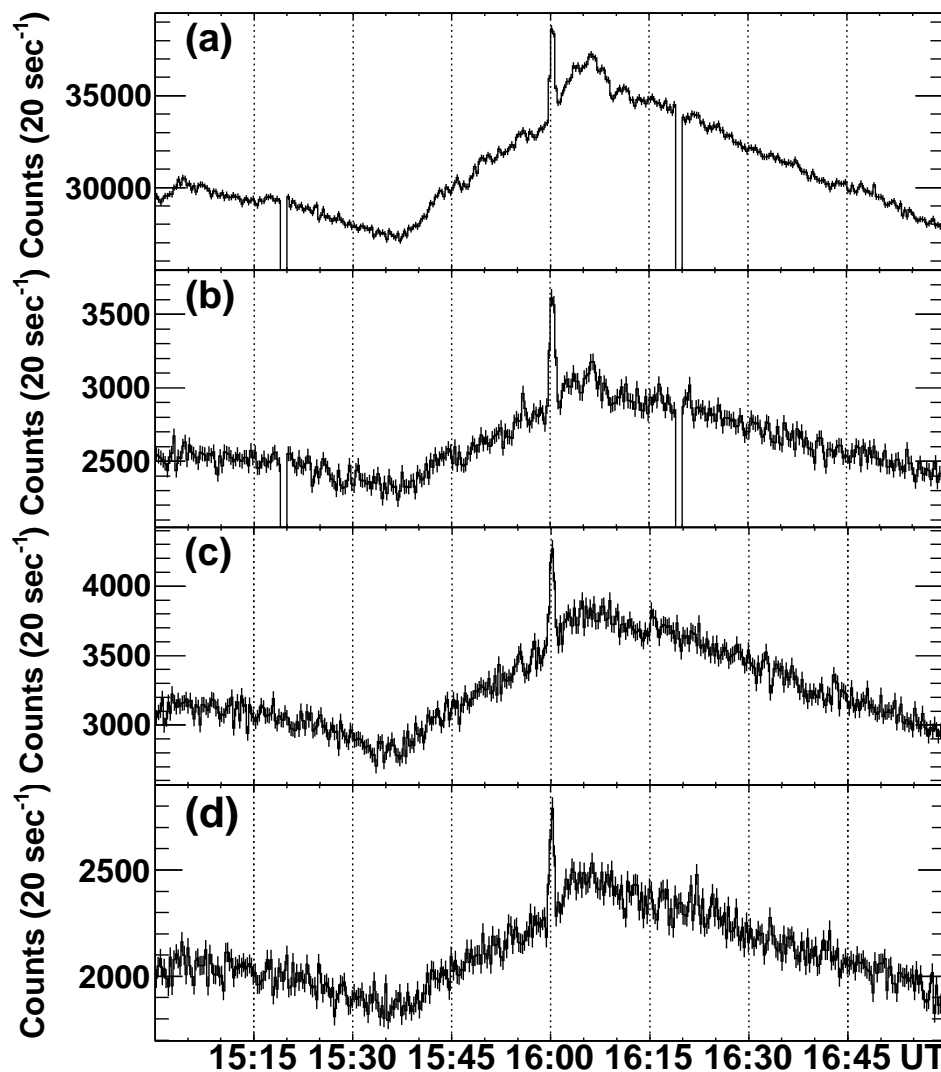


Figure 2. Count rates per 20 sec of the 4 inorganic scintillators over 15:00 – 17:00 UT on 2007 December 13. Panels (a) and (b) show the > 40 keV count rates from the BGO and NaI scintillators without the anticoincidence of Detector-A, respectively, while panels (c) and (d) represent those of NaI (> 40 keV) and CsI (> 300 keV) scintillators of Detector-B, respectively. Horizontal axis shows universal time. Error bars are statistical 1σ . The gaps in panels (a) and (b) are due to regular interruptions of data acquisition of Detector-A every hour.

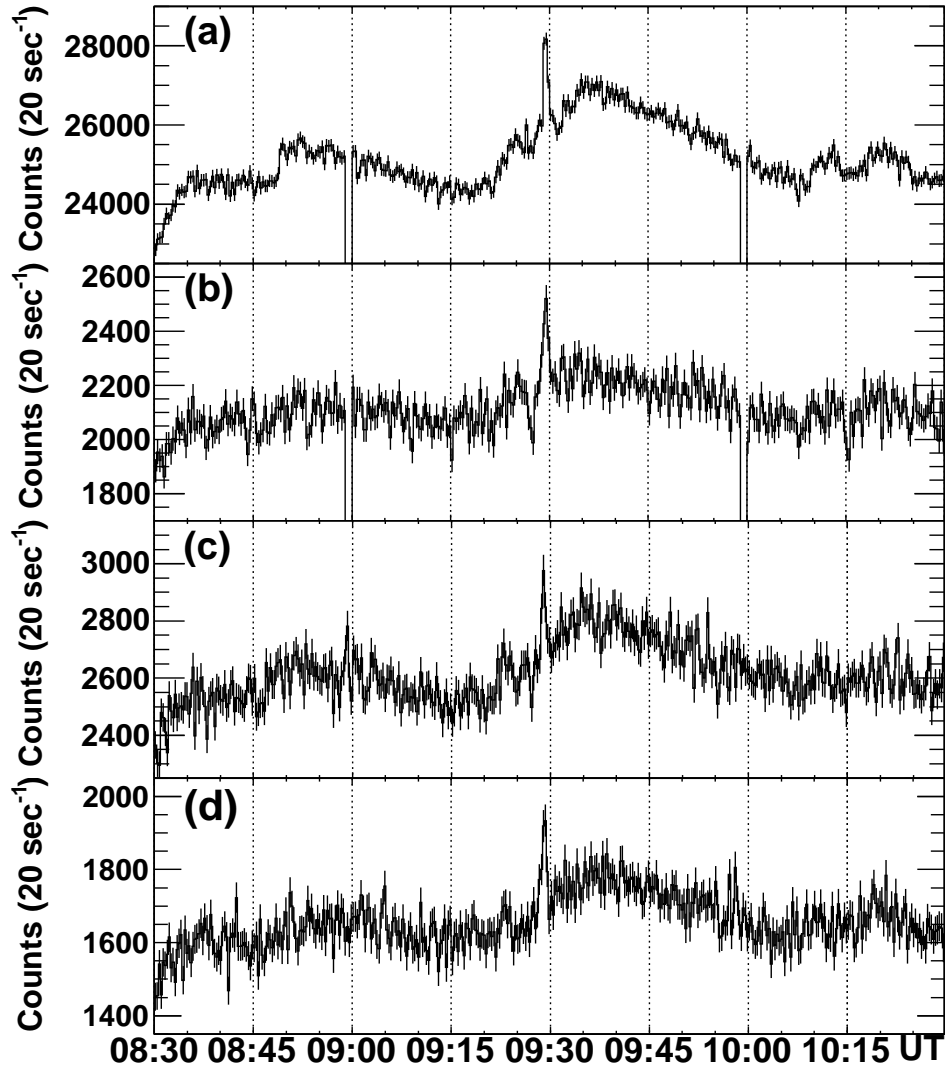


Figure 3. The same as Fig. 2, but over 8:30 – 10:30 UT on 2008 December 25.

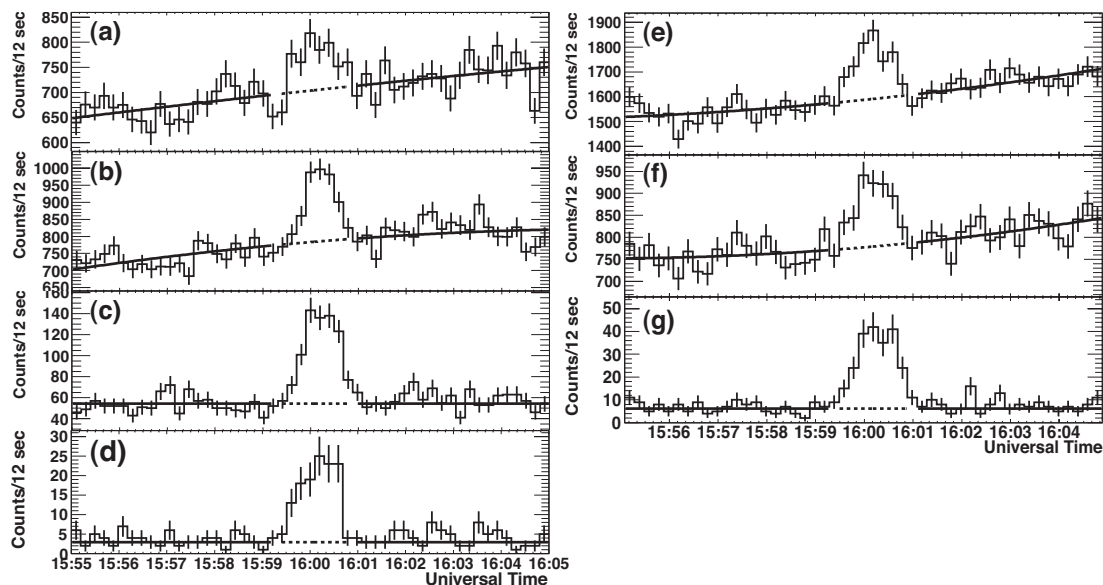


Figure 4. Count histories per 12 sec of 071213 in three energy bands from Detector-A (left; summed over the two NaI) and Detector-B (right; NaI), obtained for 15:55 – 16:05 UT. Panels (a), (b) and (c) correspond to 0.04 – 0.3 MeV, 0.3 – 3 MeV and > 3 MeV energy bands without anticoincidence, respectively. Panel (d) indicates the > 3 MeV energy band of the NaI with anticoincidence. Panels (e), (f) and (g) are the same as Panels (a), (b) and (c), respectively, but for Detector-B. Solid curves outside the burst period show the estimated background level (see text), while dashed ones denote the interpolated background level over the burst period. Abscissa represents universal time. Each error bar is statistical 1σ .

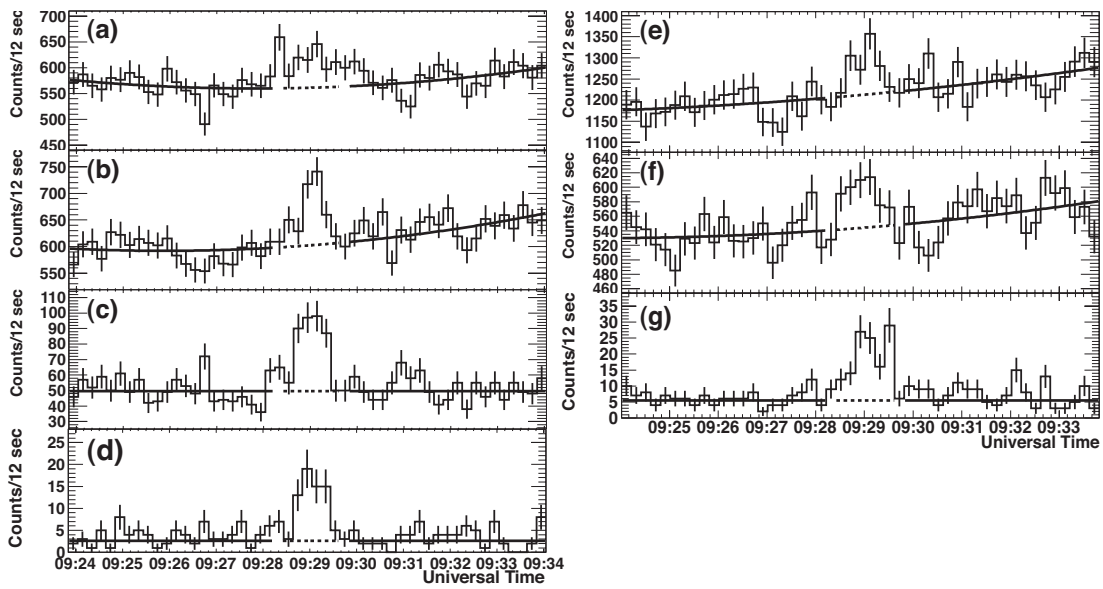


Figure 5. The same as Fig. 4, but for 081225, obtained over 9:24 – 9:34 UT.

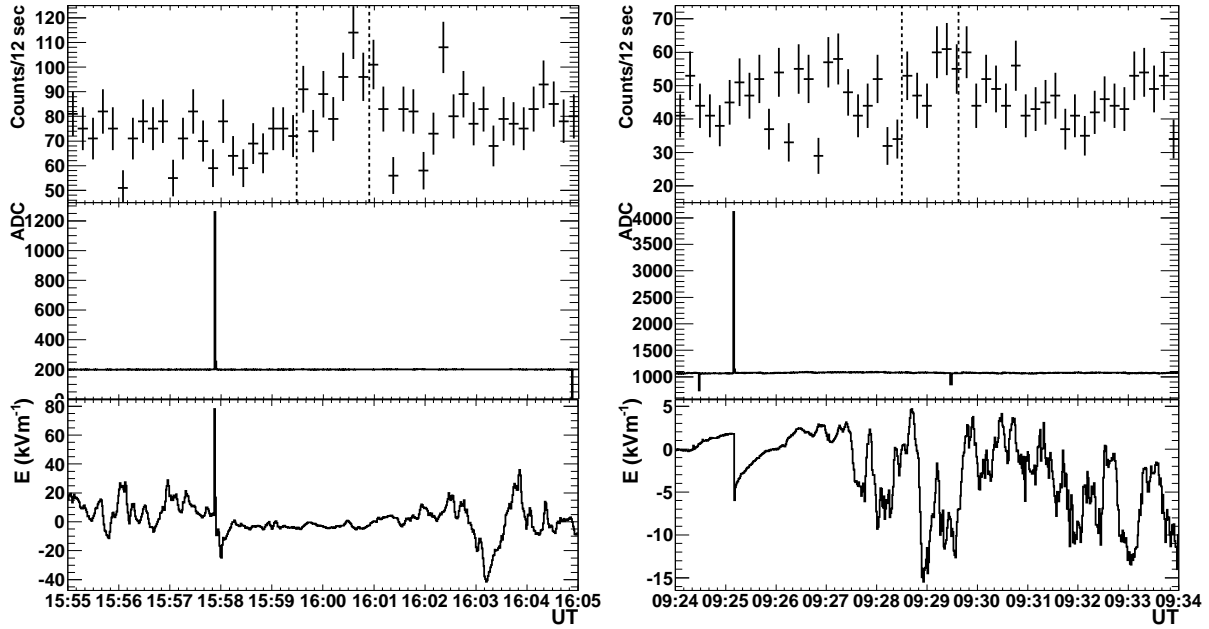


Figure 6. The count-rate histories of the plastic scintillator of Detector A and the environmental sensors. Left panels show 071213, obtained over 15:55 – 16:05 UT, while right ones represent 081225, obtained for 9:24 – 9:34 UT. Top, middle and bottom panels in both sides represent a > 1 MeV counts every 12 sec from the plastic scintillator, 1-sec optical data variations, and 1-sec electric field ones, respectively. All abscissa are universal time. Vertical lines in top panels represent the burst periods.

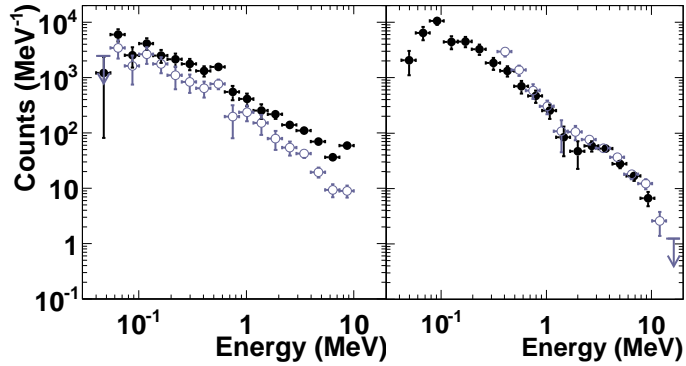


Figure 7. Background-subtracted spectra of Detector-A (left) and B (right) of 071213. Black and gray points in the left panel indicate the NaI data without and with anticoincidence, respectively, while those in the right panel show the NaI and CsI scintillators, respectively. All error bars quoted are statistical 1σ . Arrows, showing 95% confidence level upper limits, are drawing when statistical significance of a data point is lower than 1σ . The horizontal and vertical axes show the photon energy in MeV and count per unit energy interval, respectively. Detector responses have not been removed.

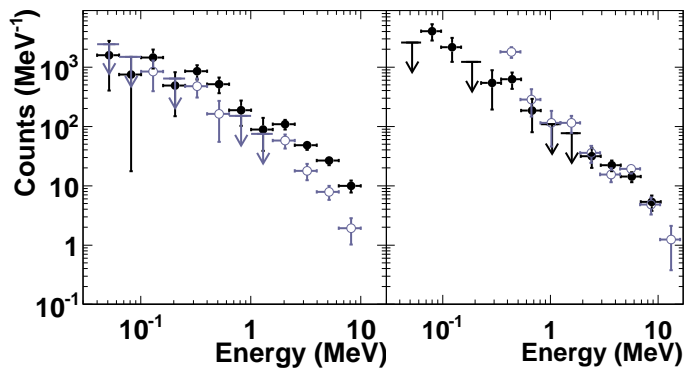


Figure 8. The same as Fig. 7, but for the 081225 event.

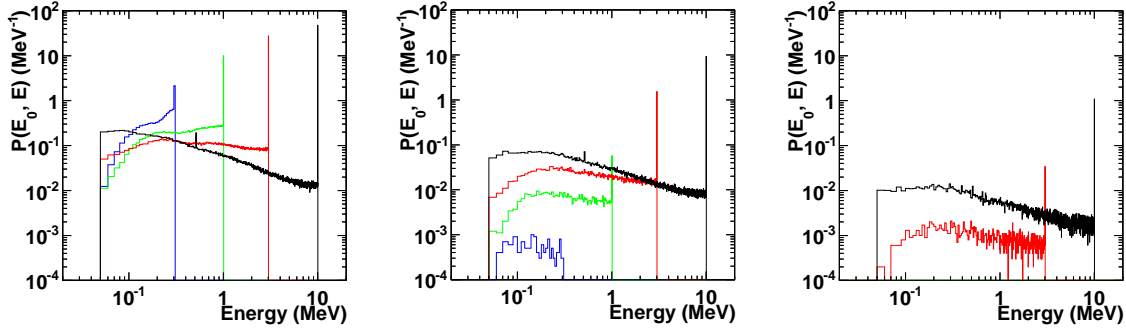


Figure 9. Photon spectra at the observatory derived from Monte Carlo simulations. Three panels correspond to $d = 300$ m (left), 1000 m (middle), and 2000 m (right). Different colors denote incident photon energies, $E_0 = 0.3$ (blue), 1 (green), 3 (red), and 10 MeV (black) in all panels. Abscissa shows the photon energy at the observatory, while ordinate represents probability density function.

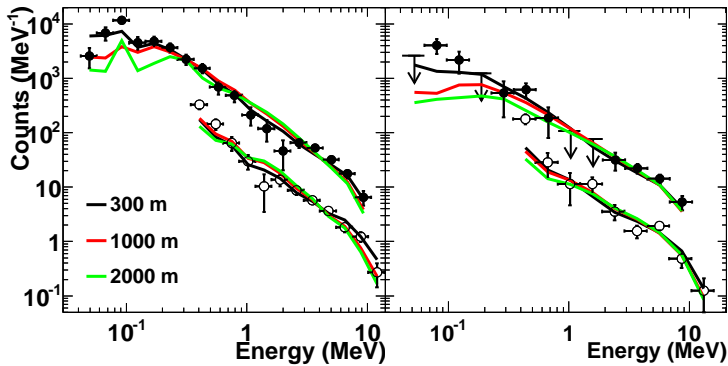


Figure 10. The photon spectra observed by the NaI (filled circles) and CsI (open circles) scintillators of Detector-B, compared with calculations for assumed source distances of 300 m (black), 1000 m (red), and 2000 m (green). Left panel shows 071213, while right one indicates 081225. For clarity, the CsI data and the corresponding model spectra are multiplied by 0.1 . The horizontal and vertical axes show the photon energy in MeV and counts in each bin, respectively.

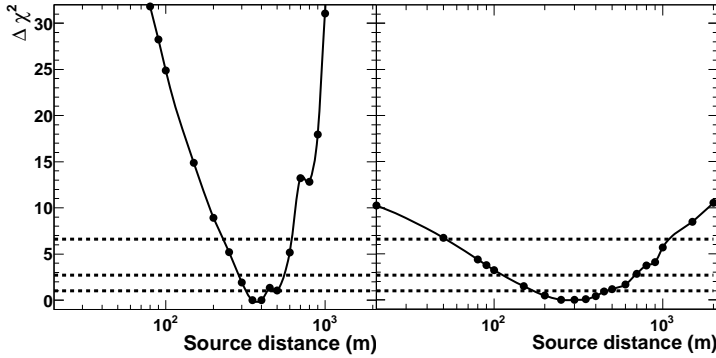


Figure 11. The values of $\Delta\chi^2 = \chi^2 - \chi_{\min}^2$, plotted as a function of the assumed source distances (black circles). Left and right panels show 071213 and 081225, respectively. Black curves show smoothing lines. Horizontal dashed lines from bottom to top correspond to 68%, 90%, and 99% confidence level.

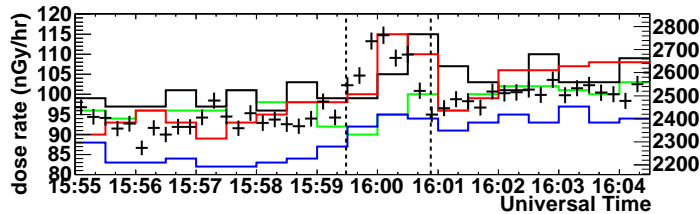


Figure 12. Radiation dose rates per 30 sec (left ordinate) obtained by ion chambers of radiation monitors over 15:55 – 16:05 UT on 2007 December 13. Different colors specify the radiation monitors numbered as 4 (green), 5 (black), 6 (red), and 7 (blue) in Fig. 1. Superposed on them, crosses show the > 40 keV count history per 12 sec of the NaI detector of Detector-B (right ordinate). Vertical dashed lines represent the defined start and end time of the 071213 event.

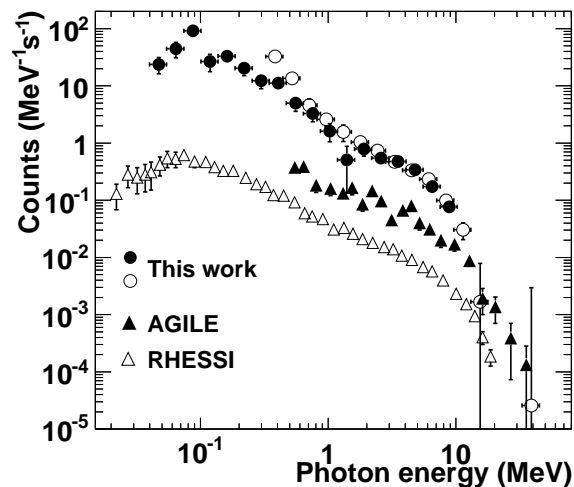


Figure 13. Cumulative spectra of the three GROWTH events from Detector-B [NaI and CsI (filled and open circles, respectively)], compared with summed TGF spectra by RHESSI and AGILE. The latter two spectra are adopted from Fig.2 of *Dwyer and Smith* [2005] and Fig.5 of *Marisaldi et al.* [2010a]. For clarity, the RHESSI and AGILE spectra are multiplied by 1×10^{-5} and 1×10^{-4} , respectively. The vertical and horizontal axes represent counts in $\text{MeV}^{-1}\text{s}^{-1}$ and photon energy in MeV, respectively. Errors assigned to the GROWTH and AGILE data are statistical ones, while those for RHESSI include systematic uncertainty of background estimation [*Dwyer and Smith*, 2005].

Table 1. The count enhancements and the corresponding photon number flux of 071213 and 081225.

ΔE (MeV)	071213			081225		
	Det. A ^a	Det. B ^b	flux ^c ($\times 10^{-2}\text{cm}^{-2}\text{s}^{-1}$)	Det. A ^a	Det. B ^b	flux ^c ($\times 10^{-2}\text{cm}^{-2}\text{s}^{-1}$)
0.04 – 0.3	530 \pm 70	1120 \pm 110	20.2 \pm 1.9	300 \pm 60	390 \pm 90	6.1 \pm 1.7
0.3 – 3	900 \pm 80	1660 \pm 140	22.2 \pm 2.3	400 \pm 60	920 \pm 110	7.6 \pm 2.1
3 – 10	410 \pm 30	370 \pm 20	10.5 \pm 1.0	180 \pm 20	178 \pm 16	6.8 \pm 0.9

^a Sum of the two NaI detectors.

^b The 0.04 – 0.3 MeV count correspond to the NaI detector, while the others a sum of the NaI and CsI detectors.

^c The flux is calculated by the data of Detector-B.

Table 2. The obtained spectral parameters and $\chi^2/\text{d.o.f.}$ of the 071213.

	P. L. ^a	Exp. P.L. ^b	Exp. P.L. (fix) ^c
α ($\text{MeV}^{-1}\text{sr}^{-1}$)	$(1.25 \pm 0.03) \times 10^{11}$	$(7.19 \pm 0.02) \times 10^{10}$	$(4.9 \pm 0.6) \times 10^9$
β	2.03 \pm 0.02	1.88 \pm 0.01	1.2 \pm 0.1
ϵ_c (MeV)	–	50 \pm 20	7
$\chi_{\min}^2/\text{d.o.f.}^{\text{d}}$	46.5/28 (1.6%)	46.0/27 (1.3%)	49.6/28 (0.72%)
d (m) ^e	400 ⁺¹⁶⁰ ₋₁₁₀	350 ⁺²¹⁰ ₋₂₄₀	150 ⁺⁶⁰ ₋₇₀

^a Power law model.

^b Exponentially cut-off power law model.

^c Exponentially cut-off power law with ϵ_c being fixed at 7 MeV.

^d Values in parentheses represent the probability with the given χ_{\min}^2 and d.o.f..

^e Quoted errors of d are 90% confidence values, while other errors are 68% ones.

Table 3. The obtained spectral parameters and $\chi^2/\text{d.o.f.}$ of 081225.

	P. L.	Exp. P.L.	Exp. P.L. (fix)
α ($\text{MeV}^{-1}\text{sr}^{-1}$)	$(1.21 \pm 0.09) \times 10^9$	$(6.4 \pm 1.0) \times 10^9$	$(5.1 \pm 0.4) \times 10^8$
β	1.61 \pm 0.03	1.48 \pm 0.09	0.87 \pm 0.02
ϵ_c (MeV)	–	70 \pm 80	7
$\chi_{\min}^2/\text{d.o.f.}$	40.9/20 (0.38%)	40.6/19 (0.25%)	43.8/20 (0.16%)
d (m)	300 ⁺³⁹⁰ ₋₁₈₀	250 ⁺⁴³⁰ ₋₂₁₀	100 ⁺²⁸⁰ ^a

^a The lower value were unable to be determined.

Table 4. The N_e estimated for 071213 and 081225.

θ_{\max} (deg.)	071213		081225	
	$H = 300$ m	$H = 1000$ m	$H = 300$ m	$H = 1000$ m
15	1.9×10^{10}	6.2×10^9	3.7×10^9	1.2×10^9
30	4.7×10^{11}	1.5×10^{11}	9.3×10^{10}	3.0×10^{10}